Metal−Graphene−Metal Sandwich Contacts for Enhanced Interface Bonding and Work Function Control

Cheng Gong,[†] David Hinojos,[†] Weichao Wang,[†] Nour Nijem,[†] Bin Shan,[†,‡] Robert M. Wallace,[†] Kyeongjae Cho,[†,*] and Yves J. Chabal[†,*]

[†]Department of Materials Science and Engineering, The University of Texas at Dallas, Richardson, Texas 75080, United States, and [‡]School of Materials Science and Engineering, Huazhong University of Science and Technology, Wuhan 430074, Hubei, China

Metal−graphene (M−G) contacts are spontaneously formed during the chemical vapor deposition (CVD) of graphene sheets on transition metal templates[1−4] and are omnipresent in graphene-based electrical devices. Interface interactions impact the structural flatness (*e.g.*, Moiré pattern)[4] of CVD-grown graphene films and the resulting contact between transferred graphene and target substrates. They also significantly affect the device electrical properties, namely, the contact resistance[5−9] and the electron−hole conduction asymmetry.[8] Moreover, the built-in electrostatic fields[10] and the hot carrier generation and transport in the contact region[11] dictate the photocurrent efficiencies and thus determine the device optoelectronic properties. Therefore, interface engineering at metal−graphene contacts is a key step toward manipulating the electrical and optoelectronic applications of graphene devices.

To date, a broad range of metals (*e.g.*, Cu, Al, Ag, Ir, Au, and Pt) have not been considered appropriate as realistic electrode materials mainly because of their weak adsorption energies on low-dimensional carbon allotropes: the carbon nanotube (CNT) and graphene. Metals have been classified into two categories based on their metal−graphene interface interaction strengths:[12−15] weak adsorption (physisorption) and strong adsorption (chemisorption) metals. Interfaces resulting from physisorption (*e.g.*, with Cu, Al, Ag, Ir, Au, and Pt) do not significantly affect the π-band dispersion of graphene but can affect its doping due to the charge transferred from/to these metals. Interfaces resulting from chemisorption (*e.g.*, with Ni, Co, Cr, Pd, and Ti) are characterized by the destruction of the graphene's π-band dispersion around the

ABSTRACT
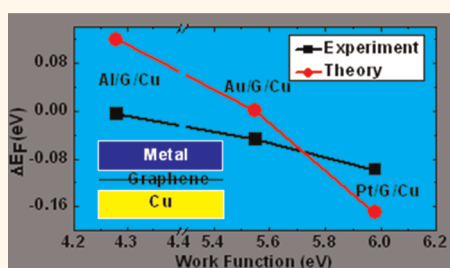
Only a small fraction of all available metals has been used as electrode materials for carbon-based devices due to metal−graphene interface debonding problems. We report an enhancement of the bonding energy of weakly interacting metals by using a metal−graphene−metal sandwich geometry, without sacrificing the intrinsic π-electron dispersions of graphene that is usually undermined by strong metal−graphene interface hybridization. This sandwich structure further makes it possible to effectively tune the doping of graphene with an appropriate selection of metals. Density functional theory calculations reveal that the strengthening of the interface interaction is ascribed to an enhancement of interface dipole−dipole interactions. Raman scattering studies of metal−graphene−copper sandwiches are used to validate the theoretically predicted tuning of graphene doping through sandwich structures.

Dirac point due to strong hybridization between metal-d and carbon-π orbitals. Consequently, metals such as Ni,[9,16] Co,[17] Cr,[17] Pd,[8,16] and Ti[8,16] have been favored as electrode materials because they form a strong bond to the graphene, although the graphene's intrinsic electronic structures are essentially destroyed. The goal is therefore to keep the intrinsic π band structure of graphene by using weakly interacting metals, yet enhance the interface stability to prevent delamination. In this work, we focus on interface engineering to exploit metals that only weakly adsorb on graphene. We

TABLE 1. Calculated Binding Energy Change (ΔBE) at M1–G (M2–G) Interfaces Due to the Presence of M2 (M1) Contacts and the Doping Levels of Graphene in Sandwich Structures[a]

M1 \ M2	Cu	Al	Ag	Ir	Au	Pt
Cu	-0.018 eV / -58.8% / 0.62eV (Cu-G: 0.47 eV)	0.004 eV / 13.8% / 9.8%	-0.010 eV / -34.2% / -33.1%	-0.014 eV / -45.8% / -41.7%	-0.004 eV / -11.7% / -9.5%	-0.019 eV / -63.8% / -41.6%
Al	0.59 (Al-G: 0.49 eV)	0.005 eV / 10.7% / 0.59eV	-0.000 eV / -0.9% / -1.2%	-0.007 eV / -15.8% / -20.1%	-0.005 eV / -10.7% / -12.2%	-0.009 / -21.4% / -19.6%
Ag	0.57 (Ag-G: 0.35 eV)	0.55 eV	-0.006 eV / -18.1% / 0.53 eV	-0.008 eV / -26.2% / -24.6%	-0.007 eV / -23.4% / -19.9%	-0.011 eV / -36.3% / -24.5%
Ir	0.19 eV (Ir-G: -0.23 eV)	0.13 eV	0.10 eV	-0.003 eV / -9.5% / -0.27 eV	-0.004 eV / -12.9% / -11.5%	-0.006 / -19.3% / -13.9%
Au	0.47 eV (Au-G: -0.20 eV)	0.37 eV	0.30 eV	-0.21 eV	-0.005 eV / -12.8% / -0.21 eV	-0.007 / -19.3% / -15.5%
Pt	0.30 eV (Pt-G: -0.31 eV)	0.19 eV	0.12 eV	-0.29 eV	-0.27 eV	-0.011 eV / -23.9% / -0.32 eV

[a] The binding energies of M1–G and M1–G/M2 structures are defined as $BE_{M1-G} = E_{M1/G} - E_{M1} - E_G$ and $BE_{M1-G/M2} = E_{M1/G/M2} - E_{M1} - E_{G/M2}$, and $\Delta BE = BE_{M1-G/M2} - BE_{M1-G} = BE_{M2-G/M1} - BE_{M2-G}$. A negative ΔBE denotes the increased interface interaction strength. Black values are the absolute ΔBE, and the red and blue values are the percentage ΔBE for M1–G (*i.e.*, $\Delta BE/BE_{M1-G}$) and M2–G (*i.e.*, $\Delta BE/BE_{M2-G}$), respectively. The doping level (green values) is the Fermi level with respect to the Dirac point ("+" sign means n-type doping of graphene). Green values in parentheses are doping levels for graphene at M1–G contacts, as a reference.

show that a sandwich structure is instrumental in achieving this goal.

For the interfaces created by weakly interacting metals, Giovannetti *et al.*[12] have shown that a transition from n-type to p-type doping of graphene takes place when the contacting metal's work function (WF) is ~5.4 eV; that is 0.9 eV larger than the intrinsic WF of graphene (~4.5 eV). They have described that the interface chemical interaction is the dominant factor for the ~0.9 eV WF discrepancies between metals and graphene, without a detailed elucidation on the mechanism of interaction. We have previously shown that the interface interaction results mainly from an interface charge repulsion effect that causes the rehybridization of metal surface atoms and the reduction of the metal WFs.[15] The consequence of the charge repulsion is that the electron density distribution tends to stay on both the metal and graphene sides, rather than being concentrated at the interface region. Thus, an interface dipole is developed, as a consequence of intramaterial (within metal and graphene respectively) charge *redistribution*, regardless of whether intermaterial (between metal and graphene) charge *transfer* takes place or not.[18] On the basis of this model, we now propose to use M1-G-M2 sandwich structures in order to modify the overall interface energy, using the

dipole–dipole interactions from both M1-G and M2-G interfaces. This sandwich structure is also expected to modify the doping type/level and thus the charge density of graphene, thus providing potential tuning of the electronic properties of graphene by selecting the top and bottom metals.

RESULTS AND DISCUSSION

Table 1 shows, through a systematic comparison among 21 M1–G–M2 sandwiches, that the sandwich structures help to improve the binding energies (BEs) at the M–G interfaces, except for the Al–G–Ag sandwich that remains almost constant and the Al–G–Cu and Al–G–Al sandwiches that both feature reduced BEs. Specifically, the BE at the Cu–G interface is increased by at least 60% due to the presence of a top Pt contact. To determine the influence of the top metal film, the band structures of Al–G–Cu (reduced BE) and Cu–G–Pt (largest increase of BE) are plotted in Figure 1. The Dirac point can be clearly resolved at the K-point in the Brillouin zone of the 2 × 2 super cell (*i.e.*, K1). The intrinsic π-band dispersion of graphene is well-preserved in these sandwich structures. Compared to the Al–G–Cu sandwich, the Cu–G–Pt sandwich is less n-type-doped because of the higher WF of Pt. Therefore, the M1–G–M2 sandwich structures
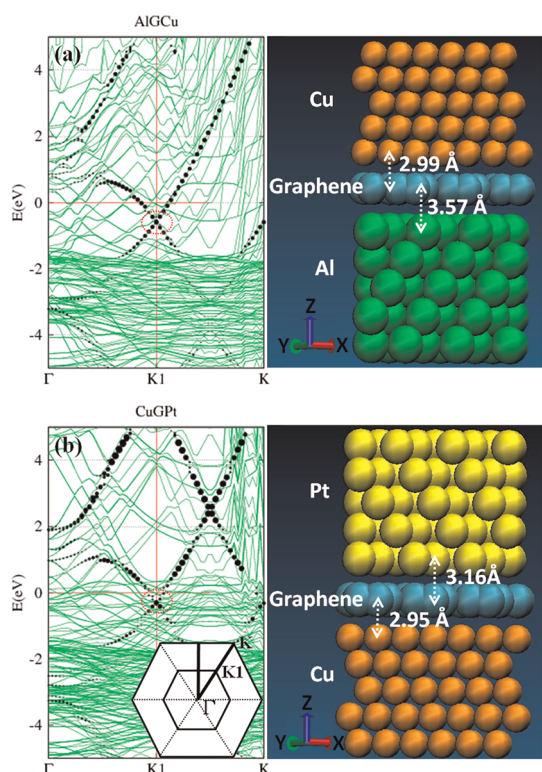
Figure 1. Band structures and schematics of Al−G−Cu (a) and Cu−G−Pt (b). The left panels are band structures, where green lines are the overall band structures and black sizable dots represent the projected character of carbon π-orbitals. In the right panels, green, orange, yellow, and cyan balls represent Al, Cu, Pt, and C atoms, respectively. K1 and K are the K-point of the Brillouin zones of 2 × 2 and 1 × 1 super cells of graphene, respectively, as shown in the inset of panel b.

Figure 2. Charge difference plot for Cu/G/Pt, Al/G/Pt, and Al/G/Cu. Charge difference $\Delta\rho = \rho(M1/G/M2) - \rho(M1) - \rho(G) - \rho(M2)$, where $\rho(M1/G/M2)$ is the charge density for M1/G/M2 sandwich contact, and $\rho(M1)$, $\rho(G)$, and $\rho(M2)$ are charge densities for isolated M1, G, and M2, respectively. All of the charge densities are averaged in the plane parallel with the interface. (b) Interface charge repulsion effects drive the charge depleting from the interface (green shaded zones) and accumulating toward the graphene (the yellow shaded zone), M1 and M2 (cyan shaded zones). The equivalent dipole formation is depicted by the depleted/accumulated charges in different zones. The intensity of charge accumulation at the graphene basal plane (the yellow shaded zone) characterizes the interface charge repulsion strength. (c) Decreasing trend (the vertical pink arrow) of the interface charge repulsion strengths (from Cu/G/Pt, the black curve, to Al/G/Cu, the orange curve), which is consistent with the relative BE changes of these sandwiches (from Cu/G/Pt, the largest BE enhancement, to Al/G/Cu, the BE reduction) as shown in Table 1.

show promise for strengthening the interface interaction without sacrificing the intrinsic electronic structure of the sandwiched graphene.

Our previous work[15] has described the interface charge repulsion occurring at metal−graphene interfaces, resulting in charge redistribution away from the interface into both metal slabs and within the graphene basal plane. Figure 2a clearly shows that the charge distribution is strongly perturbed at the interface regions of sandwich structures. The charge depletion within the intermediate regions of both M1−G and M2−G interfaces is highlighted by two green shaded zones in Figure 2b. Correspondingly, there is a charge accumulation within the graphene plane (the yellow shade zone) and in the M1 and M2 surface regions (cyan zones). The color coding in Figure 2b highlights the fact that interface charge repulsion effects play a significant role in sandwich structures.

Since both metal slabs push electrons into the carbon plane, a naive conclusion would be that the interface dipole is weakened in the sandwich structure because of the competition for the same quantum states in graphene from electrons at both surfaces. However, there is clearly a ubiquitous BE enhancement
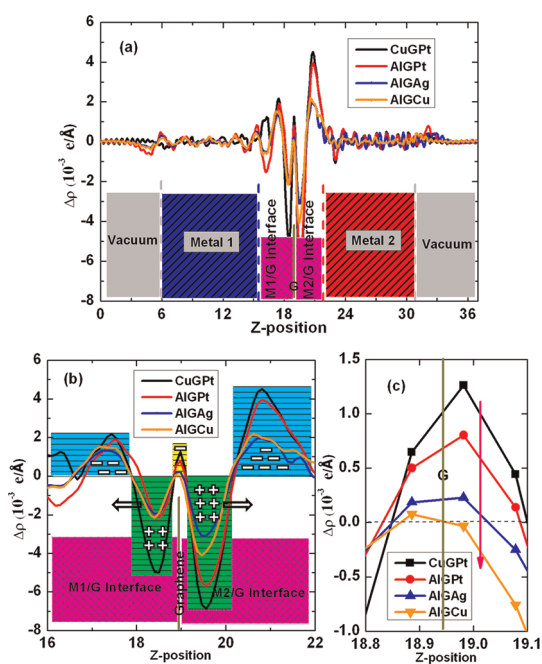
at both interfaces except for three Al-related sandwiches (*i.e.*, Al−G−Cu, Al−G−Al, and Al−G−Ag). This counterintuitive result and the dipole formation profiles in Figure 2b point to the critical role of the electron accumulation layer (EAL) at the graphene plane (highlighted by the yellow zone in Figure 2b). Without the presence of the negative charge accumulation at the graphene plane, the *antiparallel* alignment of interface dipoles would work destructively to reduce the interface binding energy (as indicated by the black arrows in Figure 2b, both pointing away from the interface to the metals). However, the presence of the EAL at the graphene basal plane allows the dipoles throughout the interfaces to interact constructively in the *parallel* alignment, due to the alternative reservoirs of opposite charges (as shown in Figure 2b). The EAL at the graphene basal plane therefore allows tuning of the interface dipoles to enhance or weaken the binding energy.

This conclusion based on the role of the EAL at the graphene basal plane is further supported by

comparing BE changes (see Table 1) of four representative sandwiches: Cu−G−Pt (40−60% BE increase), Al−G−Pt (~20% BE increase), Al−G−Ag (almost constant BE), and Al−G−Cu (~10% BE decrease). The Cu−G−Pt sandwich, with the largest BE enhancement, features the largest amount of electron accumulation at the graphene basal plane, while the Al−G−Pt sandwich, with a negligible EAL at the graphene basal plane, displays a much reduced BE. Note that the binding energy of the Al−G−Ag sandwich remains almost constant compared with single side contacts, that is, is not different from the Al−G and Ag−G binding energies (Table 1). Therefore, using this system as a reference, the electron concentration in the graphene plane of the Al−G−Cu sandwich is actually depleted, inducing a BE reduction, even though there is little charge accumulation.

There are three sandwiches without BE enhancement, all associated with the metal Al. There is a relatively larger equilibrium interface distance between Al and graphene (~3.59 Å) compared to other metals (e.g., Cu−G: 2.99 Å).[15] As previously determined by Giovannetti et al.,[12] the interface charge repulsion depends on the interface distance. The calculated Al(111) surface WF is 4.28 eV, which is 0.49 eV smaller than the calculated WF of graphene,[15] while the calculated n-type doping level of graphene in contact with Al(111) is 0.49 eV. These results indicate a negligible WF change of the Al(111) surface after attachment to graphene and thus no obvious interface charge repulsions. Giovannetti et al.[12] have a similar report for Al−graphene contacts: the WFs of Al(111) surfaces change only by 0.18 eV (from 4.22 to 4.04 eV), which is significantly less than for other metals. In the absence of intramaterial charge redistribution caused by the interface charge repulsion (e.g., for Al-related sandwiches), the intermaterial charge transfer becomes the dominant factor. This is the reason why the other three Al-related sandwiches (Al−G−Ir, Al−G−Au, and Al−G−Pt) still have enhanced BEs. The larger WF differences between Al and Ir, Au, and Pt drive the intermaterial charge transfer, thus enhancing the interface dipole.

In order to monitor the doping of graphene sandwiched by two metal slabs, the samples are characterized by Raman scattering spectroscopy. Raman spectroscopy has been used as a high-throughput and nondestructive tool not only to quantify the number of graphene layers,[19] measure the lattice strains,[20−22] and probe the electronic structures[19] of single-layer or multilayer graphene films but also to monitor the doping type and concentrations.[23−26] Despite the significant fluorescence background in Raman spectra of graphene on Cu substrates, it is still possible to derive useful information for graphene buried under several nanometers of the top metal thin films.[27,28] The analysis of the Raman spectra is based on a subtraction of the background fluorescence and a single Lorentzian peak fitting to the G and 2D bands. Due to the surface inhomogeneity of Cu substrates, a statistical average of the data collected on a 20 × 20 grid (with 1 μm intervals) is necessary to obtain reliable information at room temperature.

The samples are loaded in a cell purged by N_2 and can be annealed to 300 °C. Nitrogen purging does not cause any measurable changes in the Raman spectrum for the G/Cu system, indicating that the initial graphene surface and the G/Cu interface are not affected by ambient adsorption of O_2 and H_2O. This is in contrast to transferred graphene that is usually p-type-doped not only by chemical residues (e.g., PMMA)[29] but also by exposure to air because chemical residues provide active sites for the ambient adsorptions.[30] Nevertheless, a N_2-purge environment is still chosen for all measurements to avoid any possible perturbation by ambient gases, especially during the sample annealing process.

The reference G/Cu sample is initially annealed for 30 min to 120 °C in N_2 atmosphere to mimic the mild heating during the e-beam deposition of top metals. This annealing treatment invariably leads to a significant blue shift of the 2D peak (see Figure 3b), with a relatively negligible blue shift of the G peak (see Figure 3a). This behavior is consistent with film compression, presumably occurring upon cooling. Indeed, graphene can slide over the Cu surface when the substrate expands during annealing and is then pinned upon cooling, thereby developing regions with compressive strain and leading to blue shifts of the graphene phonon modes.

Thin metal films (~3 nm of Al, Au, and Pt) are then deposited on G/Cu to form the sandwich structures. Raman spectra are measured before and after annealing the samples 30 min at 120 °C. The negligible difference before and after the annealing proves that the sample temperature did not rise above 120 °C during e-beam evaporation.

The Raman spectra can be used to derive information on both electronic doping and lattice strain in graphene. Measuring the strain is important because strain is omnipresent from heating during the CVD growth and the metal deposition process. Once the effects of strain are determined, the data can be used to extract the doping levels of the sandwich structures. As noted, the intentional annealing of the reference samples for 30 min at 120 °C is used to mimic the heating effect during the metal deposition process. The remnants of the heating induced strain effect and the interface interaction induced morphology change in sandwich samples are further resolved by extraction of all of the strain information in Raman spectra, as explained later.

To determine the doping, the G mode frequency can be used to estimate the position of the Fermi
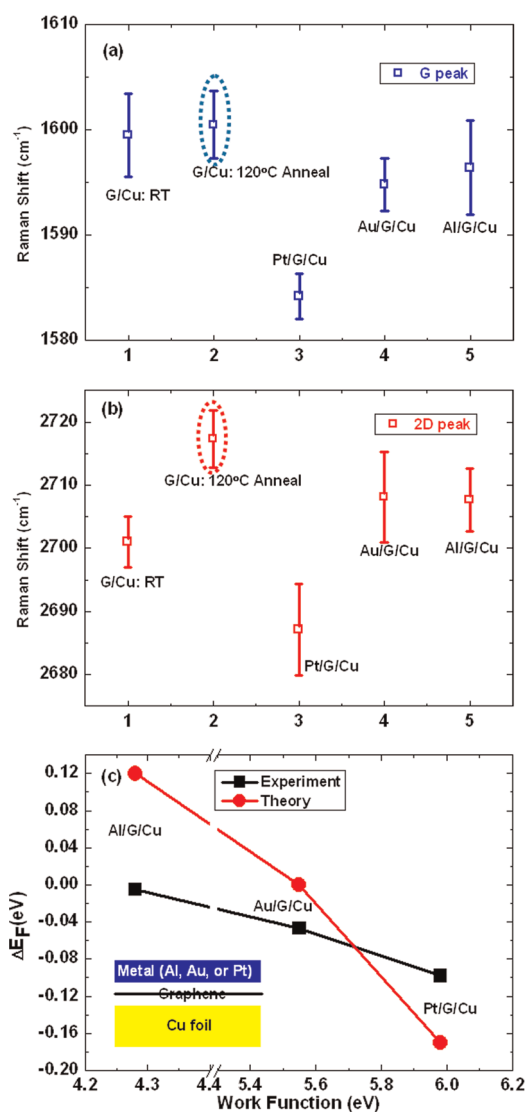
Figure 3. Raman measurement of different sandwich samples for the doping level study. (a,b) Statistical averages of G peak and 2D peak positions, respectively, for different samples. The dashed outlined sample data serve as the reference for further comparison with sandwich samples. **(c)** Comparison between simulated and experimentally extracted doping level shifts of graphene in M–G–Cu sandwich structures, with respect to the reference sample. Error bars in panels a and b represent the standard deviations of the statistical data. Inset of panel c shows the side-view schematics of M(Al, Au, or Pt)–G–Cu sandwich structures. The x-axis of panel c shows the work functions of deposited metals.

level: $\omega_G - 1580 \text{ cm}^{-1} = (42 \text{ cm}^{-1}/\text{eV}) \times |E_F|$.[24−26] Although the 2D mode shows an overall monotonic red shift with increased n-doping, the 2D dependence around the Fermi level, that is, between −0.2 eV (p-type doping) and 0.6 eV (n-type doping), is weak.[23] With regard to strain measurements, although there are discrepancies among different measurements of the Grüneisen parameters, there is a good agreement between the experimental study of Zabel et al.[22] and the combined experimental−theoretical joint work of Mohiuddin et al.[21] Previous discrepancies concerning

the Grüneisen parameter are ascribed to the different initial doping levels and strain conditions of the graphene samples due to the substrate−graphene interactions. Therefore, we chose Mohiuddin et al. and Zabel et al.'s reported value of Δ2D/ΔG (∼2.48) to describe the ratio between the shifts of the 2D and G peaks.

As discussed above, the statistically averaged Raman results of G/Cu samples at room temperature (after annealing) are considered as the reference (dashed outline in Figure 3a,b). Comparing the average positions of the 2D and G peaks between the reference and the sandwich samples, both the 2D and G peaks red shift, with the 2D peak always shifting more than the G peak. Taking the ratio between the strain induced 2D and G peaks shifts to be 2.48, and noting the linear dependence of the G peak shift on doping levels and a negligible response of the 2D peak to electronic doping close to the Fermi level, we can extract the doping component from the strain component in Raman spectra using the following steps. First, noting the larger 2D peak red shift, the strain component of the G peak shift is determined to be Δ2D/2.48; the stretched strain may be caused by the deposition induced surface roughness. Next, there is also a component of the G peak shift that is associated with the electronic doping, mainly due to the deposited metal contacts, which is therefore (ΔG − Δ2D)/2.48. Combining all of these contributions, the Fermi level shift caused by the deposited metal contact is $\Delta E_F = (\Delta G - \Delta 2D)/2.48)/(42 \text{ cm}^{-1}/\text{eV})$.

The experimentally extracted Fermi level shifts in G/Cu samples upon top metal deposition (blue curve in Figure 3c) show the same quantitative trend as the theoretically evaluated Fermi level shifts (red curve in Figure 3c). As the WFs of deposited metals increase, the Fermi levels in graphene shift down. The small discrepancies between the experimental and theoretical values in Figure 3c can be caused by many factors. First, the deposited metal layers in contact with graphene may not be crystalline with a fcc (111) grain orientation as assumed in the simulation model. Next, the M−G interface distance may not always be the same as the calculated value due to the interface roughness, impurities, and lack of commensurability. Despite these minor issues, the experimental results unambiguously show that the graphene doping (i.e., Fermi levels) can be finely tuned by the selection of M1−G−M2 sandwich structures, as predicted by DFT calculations.

CONCLUSIONS

In conclusion, the interface interactions between metals and graphene are predicted to be strengthened in most of the M1−G−M2 sandwich structures, compared with that in the conventional single-sided M−G contacts. The different dipoles formed at both M1−G

and M2–G interfaces work constructively through the electron accumulation layer at the graphene basal plane, leading to stronger interface interactions. Furthermore, the doping levels of graphene can be tuned through M1 and M2 combinations, as verified experimentally for the Al–G–Cu, Au–G–Cu, and Pt–G–Cu structures.

Although an IBM group[31] recently reported a 40% reduced contact resistance by sandwiched electrode contacts, these metal contacts are still exclusively Pd and Ti that belong to the current library of electrode materials. Our study shows that more metal species can be used in these M1–G–M2 sandwich structures, thanks to the increased interface interaction strengths, than previously considered. Therefore, many contact-related issues such as contact resistance and photocurrent generation can be revisited using a broader range of metals. For instance, the use of sandwich structures to tune the graphene contact region of transistors will help reduce the depth and length of the p–n junction[32] formation throughout the graphene channel, resulting in a decreased channel resistance.

THEORETICAL AND EXPERIMENTAL METHODS

The interface interaction strengths and electronic properties of M1–G–M2 sandwiches for six weakly interacting metals (i.e., Cu, Al, Ag, Ir, Au, and Pt) are studied theoretically by first-principles density functional theory (DFT) calculations. The contact geometries and calculation details[33,34] have been previously described for a single M–G interface model,[15] where graphene contacts metal fcc (111) surfaces. Along the vertical direction perpendicular to the interface, there is at least a 12 Å vacuum region added to minimize the interaction between neighboring super cells.

Experimentally, large graphene sheets are first grown by CVD of gaseous methane on Cu foils,[1] and then three metal species (Al, Au, and Pt) are e-beam deposited in a Temescal evaporator on the as-grown G/Cu samples to form metal/G/Cu sandwiches. The advantage of using as-synthesized G/Cu as starting materials for this study is that the graphene surface and interface are free of chemical residues that are inevitable in transferred graphene.

Micro-Raman spectrometry is used to quantify the doping behavior of graphene in sandwich structures, which is feasible due to the relatively modest thickness of the top metal film (3 nm). The sample is loaded in a Linkam FTIR600 cooling/heating stage with a continuous N_2 purge. The Raman spectra are acquired in a 20×20 square grid with a step interval 1.0 μm to obtain statistically meaningful results. The averages and standard deviations of the G and 2D peaks positions are obtained for tracking the overall structural and electronic evolutions of graphene before and after being sandwiched. A 532 nm wavelength solid-state laser is used as the source of excitation, passing through the thick transparent quartz window of the Raman cell and the 3 nm of the top metal film before being reflected by the 25 μm thick copper foils. Due to the laser power weakening in the aforementioned laser path, considering the metal substrates are good conductors for heat dissipation, and noting the previous report that there is no significant Raman spectral change when the incident power is between 0.04 and 4 mW,[19] it is safe to choose a Raman laser power of ~4.5 mW to obtain measurable intensities of the G and 2D peaks. The data from 20 scans with 2 s per scan at each spot is averaged to optimize the signal-to-noise ratio, and the data from 400 spots on each sample are taken for statistical analysis.

Conflict of Interest: The authors declare no competing financial interest.

REFERENCES AND NOTES

1. Li, X.; Cai, W.; An, J. H.; Kim, S.; Nah, J.; Yang, D.; Piner, R.; Velamakanni, A.; Jung, I.; Tutuc, E.; *et al.* Large-Area Synthesis of High-Quality and Uniform Graphene Films on Copper Foils. *Science* **2009**, *324*, 1312–1314.

2. Bae, S; Kim, H.; Lee, Y.; Xu, X.; Park, J.-S.; Zheng, Y.; Balakrishnan, J.; Lei, T.; Kim, H. R.; Song, Y.; *et al.* Role-to-Role Production of 30-in. Graphene Films for Transparent Electrodes. *Nat. Nanotechnol.* **2010**, *5*, 574–578.

3. Sutter, P. W.; Flege, J.-I.; Sutter, E. A. Epitaxial Graphene on Ruthenium. *Nat. Mater.* **2008**, *7*, 406–411.

4. N'Diaye, A. T.; Bleikamp, S.; Feibelman, P. J.; Michely, T. Two-Dimensional Ir Cluster Lattice on a Graphene Moiré on Ir(111). *Phys. Rev. Lett.* **2006**, *97*, 215501.

5. Lee, E. J. H.; Balasubramanian, K.; Weitz, R. T.; Burghard, M.; Kern, K. Contact and Edge Effects in Graphene Devices. *Nat. Nanotechnol.* **2008**, *3*, 486–490.

6. Xia, F.; Perebeinos, V.; Lin, Y.-M.; Wu, Y.; Avouris, P. The Origins and Limits of Metal–Graphene Junction Resistance. *Nat. Nanotechnol.* **2011**, *6*, 179–184.

7. Wang, X.; Ouyang, Y.; Li, X.; Wang, H.; Guo, J.; Dai, H. Room-Temperature All-Semiconducting Sub-10-nm Graphene Nanoribbon Field Effect Transistors. *Phys. Rev. Lett.* **2008**, *100*, 206803.

8. Huard, B.; Stander, N.; Sulpizio, J. A.; Goldhaber-Gordon, D. Evidence of the Role of Contacts on the Observed Electron–Hole Asymmetry in Graphene. *Phys. Rev. B* **2008**, *78*, 121402(R).

9. Venugopal, A.; Colombo, L.; Vogel, E. M. Contact Resistance in Few and Multilayer Graphene Devices. *Appl. Phys. Lett.* **2010**, *96*, 013512.

10. Xia, F.; Mueller, T.; Lin, Y.-M.; Valdes-Garcia, A.; Avouris, P. Ultrafast Graphene Photodetector. *Nat. Nanotechnol.* **2009**, *4*, 839–843.

11. Gabor, N. M.; Song, J. C. W.; Ma, Q.; Nair, N. L.; Taychatanapat, T.; Watanabe, K.; Taniguchi, T.; Levitov, L. S.; Jarillo-Herrero, P. Hot Carrier-Assisted Intrinsic Photoresponse in Graphene. *Science* **2011**, *334*, 648–652.

12. Giovannetti, G.; Khomyakov, P. A.; Brocks, G.; Karpan, V. M.; van den Brink, J.; Kelly, P. J. Doping Graphene with Metal Contacts. *Phys. Rev. Lett.* **2008**, *101*, 026803.

13. Khomyakov, P. A.; Giovannetti, G.; Rusu, P. C.; Brocks, G.; van den Brink, J.; Kelly, P. J. First-Principles Study of the Interaction and Charge Transfer between Graphene and Metals. *Phys. Rev. B* **2009**, *79*, 195425.

14. Wang, Q. J.; Che, J. G. Origins of Distinctly Different Behaviors of Pd and Pt Contacts on Graphene. *Phys. Rev. Lett.* **2009**, *103*, 066802.

15. Gong, C.; Lee, G.; Shan, B.; Vogel, E. M.; Wallace, R. M.; Cho, K. First-Principles Study of Metal–Graphene Interfaces. *J. Appl. Phys.* **2010**, *108*, 123711.

16. Robinson, J. A.; LaBella, M.; Zhu, M.; Hollander, M.; Kasarda, R.; Hughes, Z.; Trumbull, K.; Cavalero, R.; Snyder, D. Contacting Graphene. *Appl. Phys. Lett.* **2011**, *98*, 053103.

17. Nouchi, R.; Shiraishi, M.; Suzuki, Y. Transfer Chatacteristics in Graphene Field-Effect Transistors with Co Contacts. *Appl. Phys. Lett.* **2008**, *93*, 152104.

18. Bagus, P. S.; Staemmler, V.; Wöll, C. Exchangelike Effects for Closed-Shell Adsorbates: Interface Dipole and Work Function. *Phys. Rev. Lett.* **2002**, *89*, 096104.

19. Ferrari, A. C.; Meyer, J. C.; Scardaci, V.; Casiraghi, C.; Lazzeri, M.; Mauri, F.; Piscanec, S.; Jiang, D.; Novoselov, K. S.; Roth, S.; *et al.* Raman Spectrum of Graphene and Graphene Layers. *Phys. Rev. Lett.* **2006**, *97*, 187401.

20. Huang, M.; Yan, H.; Chen, C.; Song, D.; Heinz, T. F.; Hone, J. Phonon Softening and Crystallographic Orientation of Strained Graphene Studied by Raman Spectroscopy. *Proc. Natl. Acad. Sci. U.S.A.* **2009**, *106*, 7304–7308.

21. Mohiuddin, T. M. G.; Lombardo, A.; Nair, R. R.; Bonetti, A.; Savini, G.; Jalil, R.; Bonini, N.; Basko, D. M.; Galiotis, C.; Marzari, N.; *et al.* Uniaxial Strain in Graphene by Raman Spectroscopy: G Peak Splitting, Grüneisen Parameters, and Sample Orientation. *Phys. Rev. B* **2009**, *79*, 205433.

22. Zabel, J.; Nair, R. R.; Ott, A. K.; Georgiou, T.; Geim, A. K.; Novoselov, K. S.; Casiraghi, C. Raman Spectrocopy of Graphene and Bilayer under Biaxial Strain: Bubbles and Balloons. *Nano Lett.* **2012**, *12*, 617–621.

23. Das, A.; Pisana, S.; Chakraborty, B.; Piscanec, S.; Saha, S. K.; Waghmare, U. V.; Novoselov, K. S.; Krishnamurthy, H. R.; Geim, A. K.; Ferrari, A. C.; *et al.* Monitoring Dopants by Raman Scattering in an Electrochemically Top-Gated Graphene Transistor. *Nat. Nanotechnol.* **2008**, *3*, 210–215.

24. Chen, C.-F.; Park, C.-H.; Boudouris, B. W.; Horng, J.; Geng, B.; Girit, C.; Zettl, A.; Crommie, M. F.; Segalman, R. A.; Louie, S. G.; *et al.* Controlling Inelastic Light Scattering Quantum Pathways in Graphene. *Nature* **2011**, *471*, 617–620.

25. Yan, J.; Zhang, Y. B.; Kim, P.; Pinczuk, A. Electric Field Effect Tuning of Electron−Phonon Coupling in Graphene. *Phys. Rev. Lett.* **2007**, *98*, 166802.

26. Yan, H.; Xia, F.; Zhu, W.; Freitag, M.; Dimitrakopoulos, C.; Bol, A. A.; Tulevski, G.; Avouris, P. Infrared Spectroscopy of Wafer-Scale Graphene. *ACS Nano* **2011**, *5*, 9854–9860.

27. Wang, W. X.; Liang, S. H.; Yu, T.; Li, D. H.; Li, Y. B.; Han, X. F. The Study of Interaction between Graphene and Metals by Raman Spectroscopy. *J. Appl. Phys.* **2011**, *109*, 07C501.

28. Entani, S.; Sakai, S.; Matsumoto, Y.; Naramoto, H.; Hao, T.; Maeda, Y. Interface Properties of Metal/Graphene Heterostructures Studied by Micro-Raman Spectroscopy. *J. Phys. Chem. C* **2010**, *114*, 20042–20048.

29. Pirkle, A.; Chan, J.; Venugopal, A.; Hinojos, D.; Magnuson, C. W.; McDonnell, S.; Colombo, L.; Vogel, E. M.; Ruoff, R. S.; Wallace, R. M. The Effect of Chemical Residues on the Physical and Electrical Properties of Chemical Vapor Deposited Graphene Transferred to SiO_2. *Appl. Phys. Lett.* **2011**, *99*, 122108.

30. Dan, Y. P.; Lu, Y.; Kybert, N. J.; Luo, Z. T.; Johnson, A. T. C. Intrinsic Response of Graphene Vapor Sensors. *Nano Lett.* **2009**, *9*, 1472–1475.

31. Franklin, A. D.; Han, S.-J.; Bol, A. A.; Perebeinos, V. Double Contacts for Improved Performance of Graphene Transistors. *IEEE Electron Device Lett.* **2012**, *33*, 17–19.

32. Barraza-Lopez, S.; Vanevic, M.; Kindermann, M.; Chou, M. Y. Effects of Metallic Contacts on Electron Transport through Graphene. *Phys. Rev. Lett.* **2010**, *104*, 076807.

33. Kresse, G.; Furthmüller, J. Efficiency of *Ab-Initio* Total Energy Calculations for Metals and Semiconductors Using a Plane-Wave Basis Set. *J. Comput. Mater. Sci.* **1996**, *6*, 15–50.

34. Blöchl, P. E. Projector Augmented-Wave Method. *Phys. Rev. B* **1994**, *50*, 17953–17979.